# Size-dependent ferroelectric-to-paraelectric sliding transformations and antipolar-to-ferroelectric topological phase transitions in binary homobilayers

Alejandro Pacheco-Sanjuan,[1,*] Pradeep Kumar,[2,†] and Salvador Barraza-Lopez[2,3,‡]

[1]*Department of Mechanical Engineering, Universidad Técnica Federico Santa María, Valparaíso, CP 2390123, Chile*

[2]*Department of Physics, University of Arkansas, Fayetteville, Arkansas 72701, USA*

[3]*MonArk NSF Quantum Foundry, University of Arkansas, Fayetteville, Arkansas 72701, USA*

(Received 12 January 2024; accepted 18 March 2024; published 1 April 2024)

The recent discovery of ferroelectric behavior in few-layer materials, accompanied by the observation of antipolar domains in hexagonal boron nitride and transition metal dichalcogenide moiré bilayers, is paving the way for revolutionary advancements in the generation and manipulation of intrinsic electric dipoles through stacking. In addition, these cutting-edge quantum materials are reshaping our comprehension of phase transitions. Within the present paper, we unveil a size-dependent sliding behavior that marks a significant departure from conventional ferroelectrics. We also shed light on thermally induced spontaneous hyperlubric sliding within moiré bilayers, which can be used as a signal to distinguish topological phase transitions from an antipolar onto a ferroelectric bilayer. Our findings also suggest that the (topological) pinning of AA nodes in antipolar moiré homobilayers prevents the occurrence of an antipolar-to-paraelectric transformation.

DOI: 10.1103/PhysRevMaterials.8.044001

## I. INTRODUCTION

Two-dimensional (2D) ferroelectrics are fundamentally different from ternary bulk ferroelectric oxides. Those differences stem from (i) a chemistry that now includes binary [1–4] or even elemental [5–9] materials, (ii) the presence of new mechanisms for removing centers of inversion such as relative rotations within a homobilayer [2] or by the simple creation of a heterobilayer, and (iii) by the presence of ferroelectric-to-paraelectric phase transitions [10] by relative sliding [11,12] (whereby the putative paraelectric structure is a time average over ferroelectric configurations that change the direction of their intrinsic electric dipole at discrete sliding events). Bilayer ferroelectrics are created by a 60° rotation of one binary monolayer on a bilayer stack, away from a ground state configuration [2], and they feature a macroscopically large number of degenerate minima [12].

Despite the existence of works displaying double-well energy potentials [11,12] and of analytical calculations describing ferroelectric-to-paraelectric phase transitions in those homobilayers, the *size dependence* of the propensity for sliding still needs to be addressed. Furthermore, it is difficult to realize a precise 60° rotation among bilayers [13], and a more likely outcome is to achieve rotations by $60° - \delta$, where $\delta$ is a small angle. As it is well known by now, such mismatch gives rise to moirés, which have originally been studied for their unique electronic properties [14–23] but also display antipolar domains on bilayers made from binary compounds [3,10,24–28]. According to Bennett and co-workers, binary moiré homobilayers are antipolar, *not* antiferroelectric [29,30]. As superbly described by Cazeaux and co-workers, such antipolar structures feature AB and BA triangular domains separated by dislocation lines meeting at AA nodes [28]. Bennett and co-workers argue that the swap of polarization among AB and BA domains is tied to a topological winding of the local intrinsic dipole moment (which thus also includes in-plane components), with a meron and antimeron texture at AB and BA domains, respectively [31]. Such topological behavior may be readable through superlubricity, but a direct comparison of the sliding behavior of ferroelectric and antipolar bilayers has yet to be presented.

In addition, there should be a coupling of such intrinsic electric dipole with nontrivial topology to the inherent topology induced by strain in moiré hexagonal boron nitride (hBN) bilayers [25,32–34], which have one AA node per moiré supercell. *The density of domains cannot be changed spontaneously* but only by a change of the angle of rotation, strain, or a combination of both [27,28]. Atomistic reconstructions take place such that AB and BA domains occupy most of the bilayer's area, while AA nodes [28] are topological in nature [32–39], and their density per unit area cannot be modified once a relative angle of rotation has been set up. Molecular dynamics calculations were carried out at the highest allowed temperature in a molecular dynamics code to shed light on this question.

This study is based on molecular dynamics calculations, whose methodology is described in Sec. II. Results appear in Sec. III and conclusions in Sec. IV.

## II. METHODS

Atomistic models for hBN bilayers were constructed with an initial interatomic distance of 1.47 Å and an interlayer

*alejandro.pachecos@usm.cl
†pradeepk@uark.edu
‡sbarraza@uark.edu

 

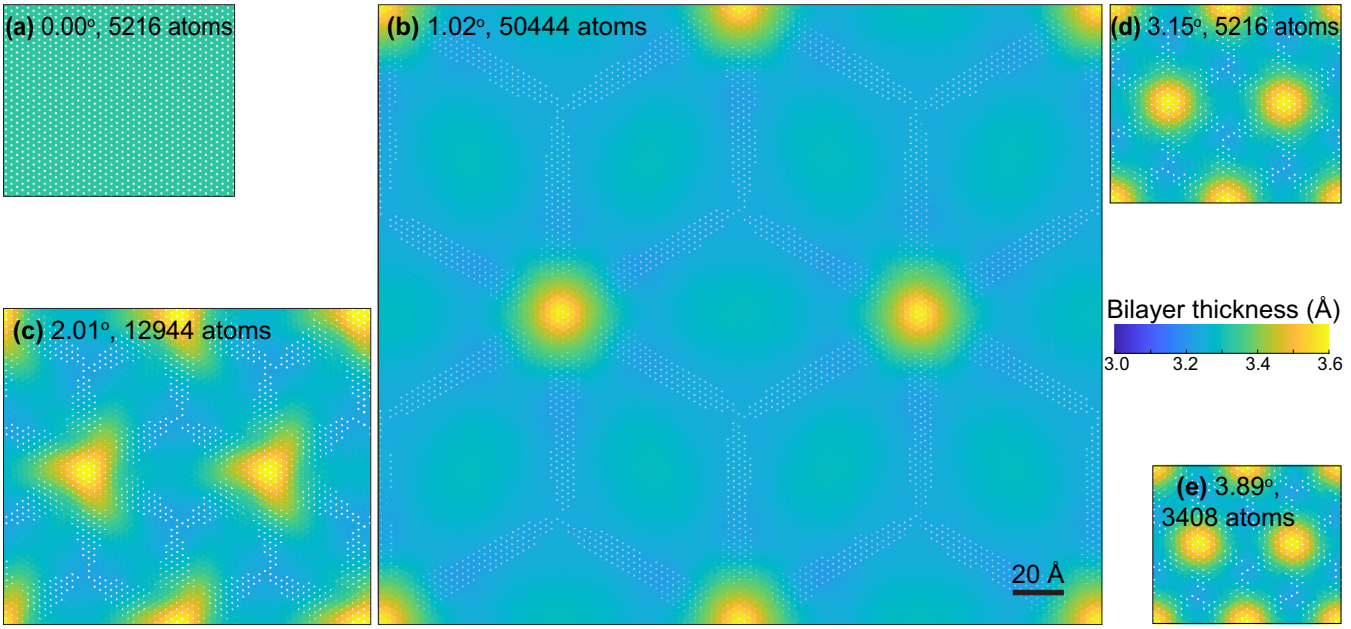


FIG. 1. Initial hBN bilayer structures after atomistic optimization at 1 K; false color indicates the relative height among layers, and the dimmest yellow locations indicate AA nodes (which are topological defects; see Ref. [27]). (a) A ferroelectric ($\delta = 0^\circ$) sample initially set into a (global) AA relative configuration. Moiré hBN bilayers with (b) $\delta = 1.02^\circ$ and 50 444 atoms, (c) $\delta = 2.01^\circ$ and 12 944 atoms, (d) $\delta = 3.15^\circ$ and 5216 atoms, and (e) $\delta = 3.89^\circ$ and 3408 atoms. All structures were drawn using the same length scale for a direct comparison.

distance of 3.33 Å. The models consisted of commensurate periodic hBN bilayers with a relative rotation angle of $60^\circ - \delta$, with $\delta = 0^\circ$ for a ferroelectric configuration, or $\delta = 1.02^\circ$, $2.01^\circ$, $3.15^\circ$, and $3.89^\circ$, for moiré antipolar configurations. The studied structures contain 50 444, 12 944, 5216, and 3408 atoms, respectively. Two additional ferroelectric bilayers with either 200 or 400 atoms were also considered to better understand the drastically different sliding behaviors of ferroelectric and antipolar bilayers.

Structures with $\delta = 0^\circ$ were initially set into an AA configuration, and forces were allowed to equilibrate in this position of (unstable) equilibrium in LAMMPS [40]. Moiré homobilayers were optimized in a similar way. Molecular dynamics simulations were performed with the same numerical tool afterwards. Intralayer energetics were described by the Tersoff potential with parameters fitted for hexagonal boron nitride (hBN) [41,42]. This interatomic potential accurately reproduces the strain energy response, equilibrium lattice constant, and phonon dispersion relations of hBN nanostructures with data obtained from x-ray scattering experiments and density functional theory (DFT) calculations. The anisotropic interlayer potential (ILP) for hBN [43] was utilized to represent interlayer interactions. The velocity Verlet scheme was used for the time integration of the resulting equations of motion with a constant time step of 0.001 ps. The interlayer energy $E_{\text{int}}$ was minimized until reaching a force threshold of $10^{-6}$ eV/Å. This permits elucidating AA nodes on moiré homobilayers, which occur at the longest interlayer separation. An $NPT$ equilibration stage (in which the number of atoms is fixed, pressure is set to 0 Pa, and temperature oscillates around 700 K) of $5 \times 10^4$ time steps was performed using the Nosé-Hoover thermostat [44,45]. Last, a "production stage" was set in an $NVE$ ensemble (where the number of atoms, the volume, and total energy remain constant) for $5 \times 10^6$ time steps (5 ns) and a sampling rate of 0.5 ps. Each monolayer's center-of-mass coordinates were recorded to detect their relative motion. Additional molecular dynamics calculations were carried out at 300 K on a moiré bilayer with a 3.15° relative rotation to determine the evolution of diffusion coefficients with temperature.

## III. RESULTS

### A. Size-dependent sliding propensity

Structures optimized in forces at zero temperature are depicted in Fig. 1. Figure 1(a) is a ferroelectric hBN bilayer ($\delta = 0^\circ$) with identical size to a moiré bilayer with $\delta = 3.15^\circ$. The green color indicates a constant relative height among monolayers for the ferroelectric configuration. Figures 1(b)–1(e) depict moiré bilayers with increasing $\delta$ (and a concomitant decrease in the number of atoms $n$). The regions in which individual constituent monolayers are farthest apart are colored in yellow. Those are energetically unfavorable AA-stacked nodes [28,46].

A precision concerning size effects and periodic boundary conditions is necessary: Even when under periodic boundary conditions, a system with $N$ atoms can only support $3N$ vibrational modes. Within the present context, the periodic boundary serves the goals of avoiding (i) dangling chemical bonds and (ii) large out-of-plane excursions commonly seen at the edges of (nonperiodic) finite-size flakes.

Figure 2 contains the first result from this work: Tang and Bauer [11] and Marmolejo-Tejada *et al.* [12] stated specific values for a critical temperature ($T_C$) on ferroelectric sliding bilayers by the onset of sliding events and—starting from

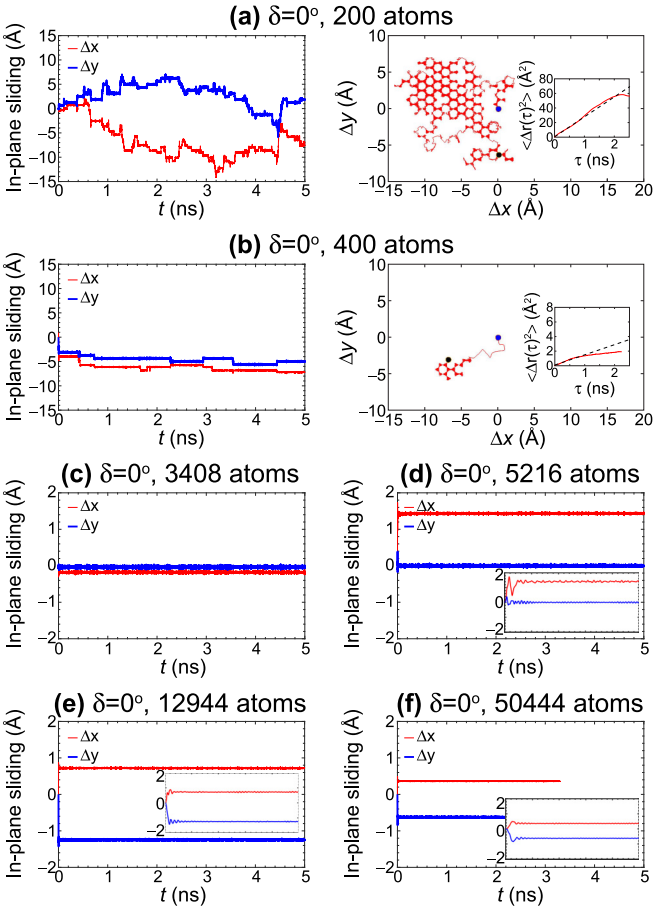


FIG. 2. Sliding of ferroelectric ($\delta = 0°$) hBN bilayers at 700 K starting from an AA relative configuration. Bilayers containing 200 and 400 atoms [(a) and (b)] undergo telegraph-noise-like discrete displacements $\Delta x$ and $\Delta y$ that sample the honeycomb lattice, similar to those described in Ref. [12]. The right panels contain the squared relative displacement of the monolayer's centers of mass as a function of time $\langle \Delta r(\tau) \rangle^2$. As bilayers increase their size [(c)–(f)], the single shear mode underpinning a whole concerted relative motion by one interatomic distance becomes suppressed, as seen by the straight lines and the comparatively smaller in-plane sliding scale. This means that a critical ferroelectric-to-paraelectric critical temperature cannot be uniquely assigned, as it depends on the bilayer's size. In (c)–(f), the bilayer quickly moves from the unstable AA configuration into stable local minima (either AB or BA), and it does not move from those local minima for the remainder of the simulation; insets show the relative displacement of one monolayer as the bilayer falls into the energy minima.

an unstable AA configuration—Figs. 2(a) and 2(b) do show discrete, telegraph-noise in-plane sliding ($\Delta x$, $\Delta y$) events [see the left panels in Figs. 2(a) and 2(b)] consistent with discrete displacements resembling the honeycomb lattice on molecular dynamics calculations at 700 K when the number of atoms is either 200 or 400 [see the sampling of the honeycomb lattice on the right subplots in Figs. 2(a) and 2(b)]. Nevertheless, the frequency of those discrete steps decreases with the number of atoms (as do the relative displacements of the center of mass) until the frequency of those displacements turns into a complete halt [see the straight lines that imply no discrete jumps on Figs. 2(c)–2(f), where the number of atoms ranges from 3408 to 50 444]. This is to say that ferroelectric bilayers by sliding should have a propensity to slide that depends not just on an inherent energy barrier, but also on the sample's size. Similar size-dependent sliding events have been reported on graphene bilayers [47].

The observed phenomena can be explained as follows: Assuming that barrier crossing can be described by a one-dimensional Smoluchowski equation [48], the rate of sliding events of ferroelectric bilayers $r_s$ could be written as

$$r_s = \frac{D\beta\omega_{\min}\omega_{\max}}{2\pi} e^{-\beta\Delta U}, \tag{1}$$

where $D$ is the diffusion coefficient (to be determined momentarily), $\beta = 1/k_B T$ is the inverse temperature, $\omega_{\min}$ and $\omega_{\max}$ are the frequencies at the minimum and the maximum of the potential well, and $\Delta U$ is the barrier height. The dependency of $D$ on the size of the bilayer, and on its ferroelectric or moiré antipolar phase, will be studied in Sec. III B

To quantify the relative sliding of monolayers seen in Figs. 2(a) and 2(b), we calculated the square of the displacement of the atom nearest to the center of mass on one monolayer as a function of time $\langle \Delta r(\tau) \rangle^2$ defined as

$$\langle \Delta r(\tau) \rangle^2 = \langle |\mathbf{r}_0(\tau + t) - \mathbf{r}_0(t)| \rangle^2 \tag{2}$$

[where $\mathbf{r}_0(t)$ is the relative sliding of the center of mass among monolayers at time $t$], and shown within the insets in the right subpanels of Figs. 2(a) and 2(b).

### B. Superlubric moiré bilayers

The main difficulty in assembling moirés is the sudden, spontaneous unwanted relative motion of monolayers [13] due to a loss of commensuration [49] upon rotation [50]. A direct comparison among Figs. 2 and 3 illustrate the different sliding behavior of ferroelectric and antipolar binary bilayers, which provides a mechanism to tell them apart.

To begin with, ferroelectric structures with 3408, 5216, 12 944, and 50 444 atoms have all commensurate unit cells containing four atoms which turn them "rougher" against relative thermally induced displacements [this is the meaning of the straight lines on Figs. 2(c)–2(f)]. The left subplots in Fig. 3 display the in-plane sliding of the two monolayers in a moiré configuration. Even though they have the same number of atoms as the structures in Figs. 2(c)–2(f), a relative sliding without discrete telegraphlike jumps can now be clearly observed. Even more, the displacements occur over a range of 100 Å, much larger than that seen in ferroelectric bilayers. The larger sliding of moiré bilayers with a lack of registry of the honeycomb lattice is evident in the right panels of Fig. 3, in which a chosen atom moves in what appears to be a continuous and random fashion.

We produced additional molecular dynamics calculations at 300 K for the bilayer at 3.15° (containing 5216 atoms) and present those results in Fig. 4. Contrasted against the results shown in Fig. 3(b), the motion is restricted at the lower temperature because the diffusion coefficient $D$ is reduced from 0.0879 Å$^2$/ps at 700 K, down to 0.0727 Å$^2$/ps at 300 K.

The differences in sliding can be further ascertained by a comparison of the slopes of the $\langle \Delta r(\tau) \rangle^2$ vs $\tau$ plots, which

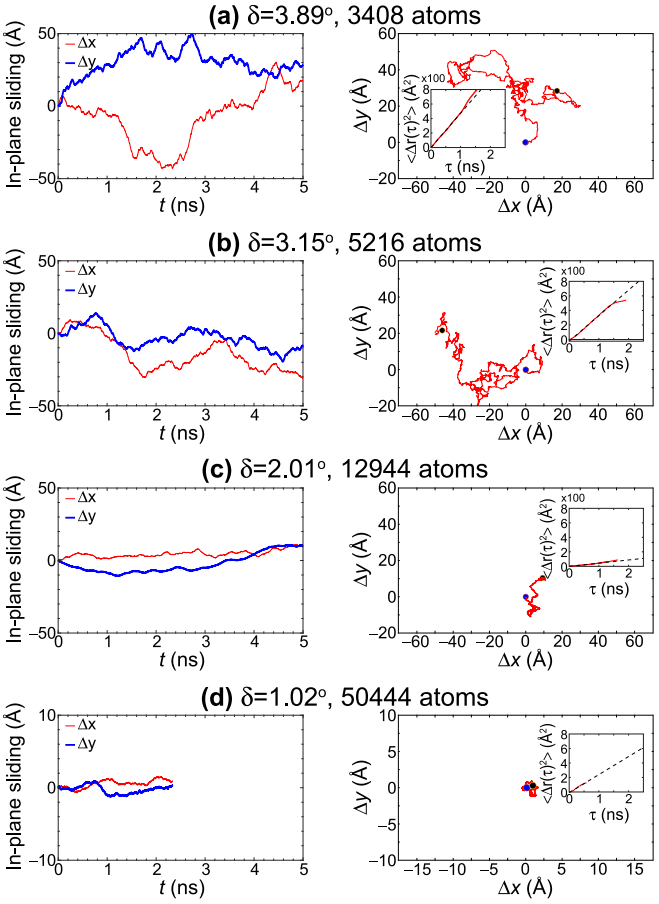


FIG. 3. Sliding of moiré hBN bilayers at 700 K. Similar to Figs. 2(a) and 2(b), the left subpanels show in-plane sliding displacements. The relative motion of the centers of mass of the individual monolayers no longer tracks the honeycomb lattice [compare the right panels to those in Figs. 2(a) and 2(b)], and the diffusion is orders of magnitude larger due to a lack of atomic registry upon relative rotation. Panels to the right contain $\langle \Delta r(\tau)\rangle^2$ as well and permit observing a suppressed diffusion as size increases.

depend on the number of atoms $n$. The idea is that, for diffusive dynamics, $\langle \Delta r(\tau)\rangle^2$ is related to the 2D diffusion constant $D(n)$ by

$$\langle \Delta r(\tau)\rangle^2 = 4D(n)\tau. \tag{3}$$

$D(n)$, plotted in Fig. 5, further confirms the striking difference in relative sliding among ferroelectric and antipolar bilayers.

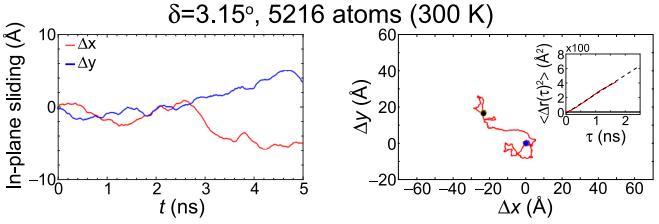


FIG. 4. Sliding of the moiré hBN bilayers with $\delta = 3.15^\circ$ at 300 K. The left subpanels show in-plane sliding displacements. The right panel contains $\langle \Delta r(\tau)\rangle^2$ and, when contrasted against Fig. 3(b), permits observing a suppressed diffusion as temperature decreases.

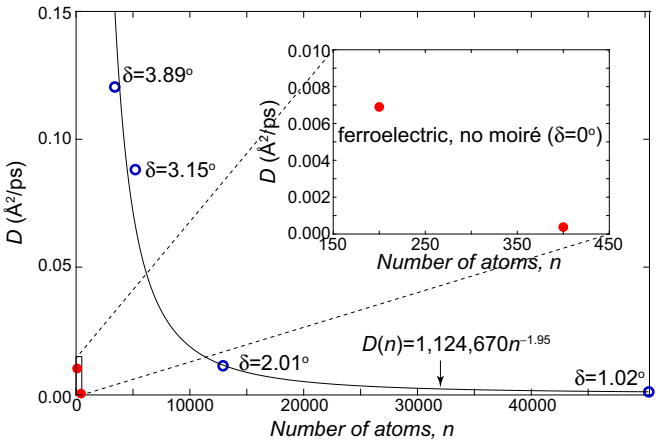


FIG. 5. Diffusion coefficient $D(n)$ obtained from the slope of $\langle \Delta r(\tau)\rangle^2 = 4D(n)\tau$. A power-law fit is included. The diffusion coefficients for two smaller ferroelectric bilayers are shown as well; note how they are orders of magnitude comparatively smaller for a given number of atoms.

In connection to the ferroelectric-to-paraelectric transition in ferroelectric bilayers by sliding, one observes a quick decay of $D$ to zero as the number of atoms increases on the ferroelectric bilayer (inset in Fig. 5). The frequency of sliding effects $r_s$ is then shown to go to zero in Eq. (1) along with $D(n)$, such that the critical temperature for a ferroelectric-to-paraelectric transition by sliding is size dependent.

An analysis of friction of moiré bilayers is provided next.

### C. Friction within moiré bilayers

We first calculate the coefficient of friction $\mu$ between the monolayers from our simulations at $T = 700$ K. $\mu$ is defined here as

$$\mu = \left\langle \frac{F_f}{F_z} \right\rangle, \tag{4}$$

where $F_z \geqslant 0$ and $F_f$ are the instantaneous normal and friction forces, respectively, and $\langle\cdot\rangle$ denotes a time average. The variation of $\langle F_z\rangle$, $\langle F_f\rangle$, average interlayer energy $\langle E_{\rm int}\rangle$, and the coefficient of friction $\mu$ as a function of the number of atoms $n$ (and, implicitly, on the relative rotation angle $\delta$) for moiré hBN bilayers are depicted in Fig. 6. The friction and normal forces increase with $n$, but they follow different trends. The coefficient of friction remains in the superlubricity regime ($\mu < 0.01$) [51] for all values of $n$ ($\delta$). Rue *et al.* determined $\mu = 0.005$ for $MoS_2/MoSe_2$ heterostructures [52] at 300 K for $\delta = 5^\circ$ and $\langle F_z\rangle = 0.2$ nN/atom. In our calculations at 700 K and for the largest angle we studied ($\delta = 3.89^\circ$), $\langle F_z\rangle = 0.0183$ nN/atom, and the coefficient of friction was 0.0016, which is comparable with that of the $MoS_2/MoSe_2$ heterostructure.

At this point, we use the Green-Kubo formalism to calculate the interlayer friction constant λ. There, the interlayer friction constant λ is defined as [53–57]

$$\lambda = \lim_{t\to\infty} \frac{1}{2k_BTA} \int_0^t c(t')dt', \tag{5}$$

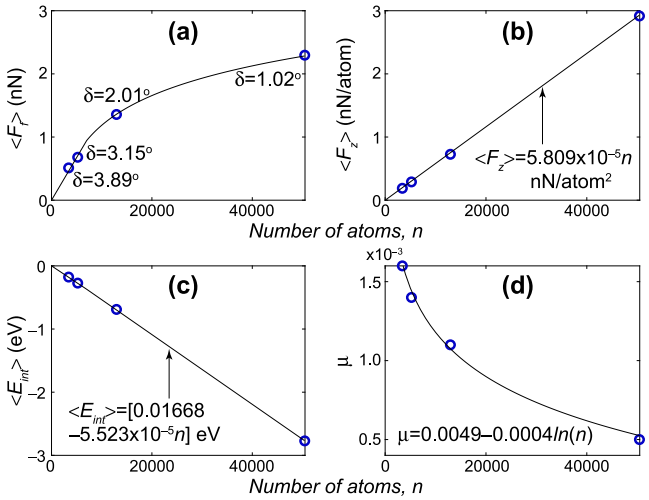


FIG. 6. Dependence of (a) average friction force $\langle F_f \rangle$, (b) average normal force $\langle F_N \rangle$, (c) average interlayer energy $\langle E_{\rm int} \rangle$, and (d) coefficient of friction $\mu$ on the number of atoms (i.e., on the angle $\delta$) for moiré hBN bilayers. The recorded values of $\mu$ imply that these are superlubric.

where $k_B$ is the Boltzmann constant, $T$ is the temperature, $A$ is the contact area, and $c(t)$ is the lateral (in-plane) force correlation function defined as

$$c(t) = \langle \mathbf{F}_\parallel(t)\mathbf{F}_\parallel(0)\rangle. \tag{6}$$

The force autocorrelation function $c(t)$ is shown in Fig. 7(a) for moiré hBN bilayers of different sizes ($\delta$) at $T = 700$ K. For all values of $n$, $c(t)$ decreases rapidly and decays to zero at a timescale of order of 200 ps. In order to investigate the frequency response of the friction constant, we next looked the Fourier transform of $c(t)$:

$$c(\omega) = \int_0^\infty c(t)e^{-i\omega t}dt. \tag{7}$$

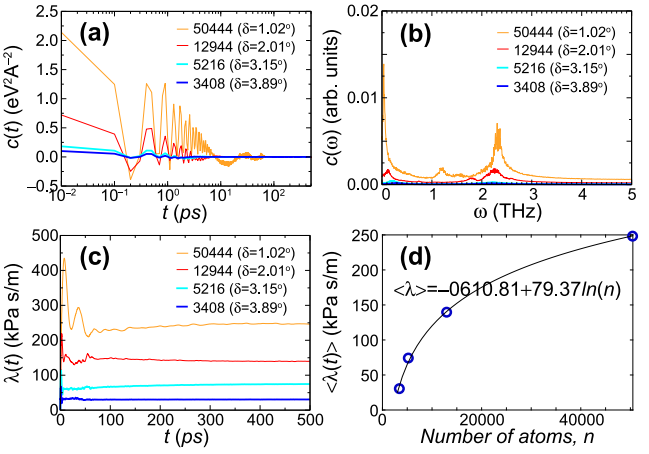


FIG. 7. (a) Time autocorrelation of the lateral force between the monolayers. (b) Fourier transform of the force autocorrelation function. (c) Time dependence of $\lambda(t)$. (d) Friction constant $\lambda$ as a function of the number of atoms $n$.

$c(\omega)$ was calculated for different values of $\delta$ in Fig. 7(b). We find that $c(\omega)$ exhibits two peaks—one at lower frequency (≈0.1 THz), and another at slightly higher frequency (≈2.0 THz). The amplitude of the lower-frequency peak becomes smaller and moves to slightly higher frequency, while the amplitude of the high-frequency peak becomes weaker upon decreasing $n$. In Fig. 7(c), we show the behavior of $\lambda(t)$ for four different values of $n$. The values of the friction constant obtained from the long-time behavior of $\lambda(t)$ are shown as a function of $n$ in Fig. 7(d); $\lambda$ increases monotonically with increasing $n$. The behavior of the friction constant is consistent with the increasing value of friction force with $n$ discussed in Fig. 6(a).

### D. Observations on an antipolar-to-paraelectric phase transitions

AB and BA domains on moiré bilayers form a network separated by dislocation lines meeting at AA nodes [27,28]. Engelke and coauthors posited that one can map the local relative sliding configurations in individual unit cells though the moiré into a closed space akin to a punctured torus, where the punctured section is precisely the AA node. In this map, the torus is the closed surface in which the winding of a local displacement field turns out to be topological [27]. And so, the last item for discussion is the possibility of a mechanism by which the density of topologically protected AA nodes alluded to above [27,28] could be thermally altered. That possibility was the reason to perform molecular dynamics calculations at 700 K in the first place (which was the highest we could achieve without facing numerical instabilities in the code).

Figure 8 presents a qualitative answer to the question. Figures 8(a)–8(c) show the relative height among the two monolayers in the $\delta = 1.02^\circ$ configuration at three different times (2.05, 2.15, and 2.30 ns) along the molecular dynamics evolution. The darkest hue is a 3.5 Å cutoff, above which the local bilayer has a local AA stacking. Similarly, Figs. 8(d)–8(f) display the moiré bilayer at 700 K when $\delta = 2.01^\circ$ at the following simulation times: 4.295, 4.345, 4.395 ns. The point is that, though those move around, *four* AA-stacked sections always remain visible on the snapshots.

We just showed by molecular dynamics calculations that the AA nodes cannot be thermally removed. Therefore, to produce a transition onto a ferroelectric or paraelectric phase, the only options are either (i) a quantum phase transition, or (ii) a topological one. As the temperature is high, a quantum phase transition is discarded as well, and a topological transition signified by the removal of AA nodes is the only possibility left. Indeed, the rotation by $-\delta$ renders the antipolar moiré onto a ferroelectric configuration which may be unstable to sliding events depending on the samples' size and temperature.

## IV. CONCLUSION

To conclude, we undertook a study of hBN bilayers in the ferroelectric ($\delta = 0^\circ$) and moiré antipolar ($\delta > 0^\circ$) configurations. We first established the fact that ferroelectric-to-paraelectric transitions by sliding occur at temperatures dependent on system size. Then, using configurations with

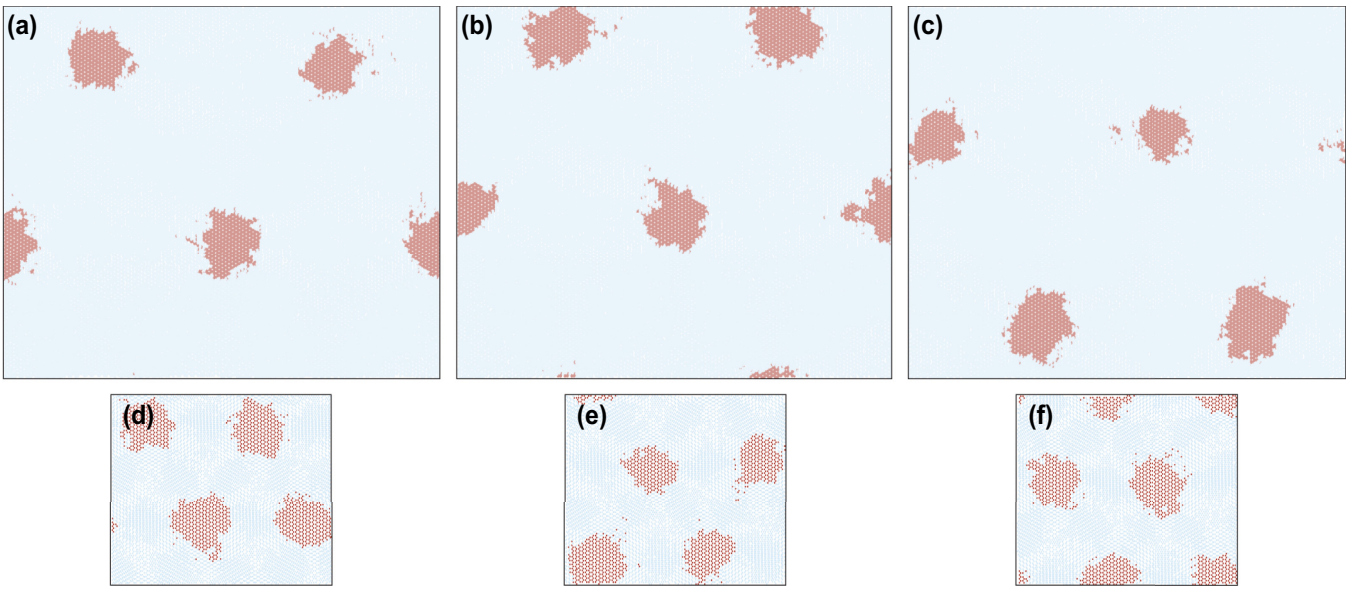


FIG. 8. The number of topological defects (dark-colored patches corresponding to AA-stacked sections [27,28]) for the moiré hBN bilayer with $\delta = 1.02^\circ$ at (a) 2.05 ns, (b) 2.15 ns, and (c) 2.30 ns and at 700 K. (d)–(f) display the moiré bilayer at 700 K at $2.01^\circ$ at 4.295, 4.345, and 4.395 ns, respectively. In both cases, a diameter of about 50 Å can be observed for the AA nodes.

an identical number of atoms, we found an easier propensity to slide of antipolar moiré bilayers. This study included the calculation of the diffusion coefficient, and of parameters $\mu$ and $\lambda$ that indicate superlubric behavior. The work ends by the observation that the area density of topological defects (given by AA nodes) remains protected at the highest temperature of 700 K, in which molecular dynamics simulations could run without developing numerical instabilities. Therefore, the only possibility for the removal of AA nodes is a rotation out of the topologically nontrivial moiré conformation onto a (trivial) configuration with a single realization of relative sliding among monolayers across all unit cells.

## ACKNOWLEDGMENTS

S.B.-L. acknowledges funding from the U.S. Department of Energy (Award No. DE-SC0022120).

[1] K. Chang, J. Liu, H. Lin, N. Wang, K. Zhao, A. Zhang, F. Jin, Y. Zhong, X. Hu, W. Duan *et al.*, Science **353**, 274 (2016).
[2] L. Li and M. Wu, ACS Nano **11**, 6382 (2017).
[3] Q. Yang, M. Wu, and J. Li, J. Phys. Chem. Lett. **9**, 7160 (2018).
[4] S. Barraza-Lopez, B. M. Fregoso, J. W. Villanova, S. S. P. Parkin, and K. Chang, Rev. Mod. Phys. **93**, 011001 (2021).
[5] C. Xiao, F. Wang, S. A. Yang, Y. Lu, Y. Feng, and S. Zhang, Adv. Funct. Mater. **28**, 1707383 (2018).
[6] J. Gou, H. Bai, X. Zhang, Y. L. Huang, S. Duan, A. Ariando, S. A. Yang, L. Chen, Y. Lu, and A. T. S. Wee, Nature (London) **617**, 67 (2023).
[7] A. Garcia-Ruiz, V. Enaldiev, A. McEllistrim, and V. I. Fal'ko, Nano Lett. **23**, 4120 (2023).
[8] L. Yang, S. Ding, J. Gao, and M. Wu, Phys. Rev. Lett. **131**, 096801 (2023).
[9] S. S. Atri, W. Cao, B. Alon, N. Roy, M. V. Stern, V. Fal'ko, M. Goldstein, L. Kronik, M. Urbakh, O. Hod, and M. B. Shalom, Adv. Phys. Res. 2300095 (2024).
[10] Y. Liu, S. Liu, B. Li, W. J. Yoo, and J. Hone, Nano Lett. **22**, 1265 (2022).
[11] P. Tang and G. E. W. Bauer, Phys. Rev. Lett. **130**, 176801 (2023).
[12] J. M. Marmolejo-Tejada, J. E. Roll, S. P. Poudel, S. Barraza-Lopez, and M. A. Mosquera, Nano Lett. **22**, 7984 (2022).
[13] C. N. Lau, M. W. Bockrath, K. F. Mak, and F. Zhang, Nature (London) **602**, 41 (2022).
[14] J. M. B. Lopes dos Santos, N. M. R. Peres, and A. H. Castro Neto, Phys. Rev. Lett. **99**, 256802 (2007).
[15] G. Li, A. Luican, J. M. B. Lopes dos Santos, A. H. Castro Neto, A. Reina, J. Kong, and E. Y. Andrei, Nat. Phys. **6**, 109 (2010).
[16] G. Trambly de Laissardiére, D. Mayou, and L. Magaud, Nano Lett. **10**, 804 (2010).
[17] E. Suárez Morell, J. D. Correa, P. Vargas, M. Pacheco, and Z. Barticevic, Phys. Rev. B **82**, 121407(R) (2010).
[18] M. H. Naik and M. Jain, Phys. Rev. Lett. **121**, 266401 (2018).
[19] F. Wu, T. Lovorn, E. Tutuc, and A. H. MacDonald, Phys. Rev. Lett. **121**, 026402 (2018).
[20] J. He, K. Hummer, and C. Franchini, Phys. Rev. B **89**, 075409 (2014).
[21] Y. Zhang, N. F. Q. Yuan, and L. Fu, Phys. Rev. B **102**, 201115(R) (2020).
[22] L. Wang, E.-M. Shih, A. Ghiotto, L. Xian, D. A. Rhodes, C. Tan, M. Claassen, D. M. Kennes, Y. Bai, B. Kim *et al.*, Nat. Mater. **19**, 861 (2020).
[23] L. Xian, D. M. Kennes, N. Tancogne-Dejean, M. Altarelli, and A. Rubio, Nano Lett. **19**, 4934 (2019).
[24] J. Park, I. W. Yeu, G. Han, C. S. Hwang, and J.-H. Choi, Sci. Rep. **9**, 14919 (2019).

[25] X. Wang, K. Yasuda, Y. Zhang, S. Liu, K. Watanabe, T. Taniguchi, J. Hone, L. Fu, and P. Jarillo-Herrero, Nat. Nanotechnol. **17**, 367 (2022).
[26] M. Wu and J. Li, Proc. Natl. Acad. Sci. USA **118**, e2115703118 (2021).
[27] R. Engelke, H. Yoo, S. Carr, K. Xu, P. Cazeaux, R. Allen, A. M. Valdivia, M. Luskin, E. Kaxiras, M. Kim *et al.*, Phys. Rev. B **107**, 125413 (2023).
[28] P. Cazeaux, D. Clark, R. Engelke, P. Kim, and M. Luskin, J. Elast. **154**, 443 (2023).
[29] D. Bennett and B. Remez, npj 2D Mater. Appl. **6**, 7 (2022).
[30] D. Bennett, Phys. Rev. B **105**, 235445 (2022).
[31] D. Bennett, G. Chaudhary, R.-J. Slager, E. Bousquet, and P. Ghosez, Nat. Commun. **14**, 1629 (2023).
[32] C. R. Woods, P. Ares, H. Nevison-Andrews, M. J. Holwill, R. Fabregas, F. Guinea, A. K. Geim, K. S. Novoselov, N. R. Walet, and L. Fumagalli, Nat. Commun. **12**, 347 (2021).
[33] K. Yasuda, X. Wang, K. Watanabe, T. Taniguchi, and P. Jarillo-Herrero, Science **372**, 1458 (2021).
[34] M. Vizner Stern, Y. Waschitz, W. Cao, I. Nevo, K. Watanabe, T. Taniguchi, E. Sela, M. Urbakh, O. Hod, and M. B. Shalom, Science **372**, 1462 (2021).
[35] H. Yoo, R. Engelke, S. Carr, S. Fang, K. Zhang, P. Cazeaux, S. H. Sung, R. Hovden, A. W. Tsen, T. Taniguchi *et al.*, Nat. Mater. **18**, 448 (2019).
[36] S. G. Xu, A. I. Berdyugin, P. Kumaravadivel, F. Guinea, R. Krishna Kumar, D. A. Bandurin, S. V. Morozov, W. Kuang, B. Tsim, S. Liu *et al.*, Nat. Commun. **10**, 4008 (2019).
[37] S. L. Moore, C. J. Ciccarino, D. Halbertal, L. J. McGilly, N. R. Finney, K. Yao, Y. Shao, G. Ni, A. Sternbach, E. J. Telford *et al.*, Nat. Commun. **12**, 5741 (2021).
[38] A. Weston, Y. Zou, V. Enaldiev, A. Summerfield, N. Clark, V. Zólyomi, A. Graham, C. Yelgel, S. Magorrian, M. Zhou *et al.*, Nat. Nanotechnol. **15**, 592 (2020).
[39] M. Van Winkle, I. M. Craig, S. Carr, M. Dandu, K. C. Bustillo, J. Ciston, C. Ophus, T. Taniguchi, K. Watanabe, A. Raja, S. M. Griffin, and D. Kwabena Bediako, Nat. Commun. **14**, 2989 (2023).
[40] S. Plimpton, J. Comput. Phys. **117**, 1 (1995).
[41] A. Kınacı, J. B. Haskins, C. Sevik, and T. Çağın, Phys. Rev. B **86**, 115410 (2012).
[42] C. Sevik, A. Kinaci, J. B. Haskins, and T. Çağin, Phys. Rev. B **84**, 085409 (2011)
[43] W. Ouyang, D. Mandelli, M. Urbakh, and O. Hod, Nano Lett. **18**, 6009 (2018).
[44] W. G. Hoover, Phys. Rev. A **31**, 1695 (1985).
[45] S. Nosé, J. Chem. Phys. **81**, 511 (1984).
[46] S. Zhou, J. Han, S. Dai, J. Sun, and D. J. Srolovitz, Phys. Rev. B **92**, 155438 (2015).
[47] S. Bagchi, H. T. Johnson, and H. B. Chew, Phys. Rev. B **101**, 054109 (2020).
[48] R. Zwanzig, *Nonequilibrium Statistical Mechanics* (Oxford University Press, Oxford, UK, 2001).
[49] M. Hirano and K. Shinjo, Phys. Rev. B **41**, 11837 (1990).
[50] M. Dienwiebel, G. S. Verhoeven, N. Pradeep, J. W. M. Frenken, J. A. Heimberg, and H. W. Zandbergen, Phys. Rev. Lett. **92**, 126101 (2004).
[51] M. H. Müser, in *Fundamentals of Friction and Wear on the Nanoscale*, edited by E. Gnecco and E. Meyer (Springer, Berlin, 2014), pp. 209–232.
[52] G. Ru, W. Qi, K. Tang, Y. Wei, and T. Xue, Tribol. Int. **151**, 106483 (2020).
[53] R. Kubo, J. Phys. Soc. Jpn. **12**, 570 (1957).
[54] J. G. Kirkwood, J. Chem. Phys. **14**, 180 (1946).
[55] L. Bocquet and J.-L. Barrat, J. Chem. Phys. **139**, 044704 (2013).
[56] M. Panoukidou, C. R. Wand, and P. Carbone, Soft Matter **17**, 8343 (2021).
[57] S. Shkulipa, W. K. den Otter, and W. J. Briels, Biophys. J. **89**, 823 (2005).